

Physical mechanisms of phonation onset: A linear stability analysis of an aeroelastic continuum model of phonation

Zhaoyan Zhang, Juergen Neubauer, David A. Berry, and AL

Citation: [The Journal of the Acoustical Society of America](#) **122**, 2279 (2007); doi: 10.1121/1.2773949

View online: <http://dx.doi.org/10.1121/1.2773949>

View Table of Contents: <http://asa.scitation.org/toc/jas/122/4>

Published by the [Acoustical Society of America](#)

Articles you may be interested in

[Asymmetric airflow and vibration induced by the Coanda effect in a symmetric model of the vocal folds](#)
122, (2007); 10.1121/1.2773960

[Modeling of chaotic vibrations in symmetric vocal folds](#)

The Journal of the Acoustical Society of America **110**, 2120 (2001); 10.1121/1.1395596

[The minimum glottal airflow to initiate vocal fold oscillation](#)

121, (2007); 10.1121/1.2710961

[Modeling coupled aerodynamics and vocal fold dynamics using immersed boundary methods](#)

120, (2006); 10.1121/1.2354069

[A contribution to simulating a three-dimensional larynx model using the finite element method](#)

The Journal of the Acoustical Society of America **114**, 2893 (2016); 10.1121/1.1619981

[Modeling vocal fold motion with a hydrodynamic semicontinuum model](#)

The Journal of the Acoustical Society of America **114**, 455 (2003); 10.1121/1.1577547

Physical mechanisms of phonation onset: A linear stability analysis of an aeroelastic continuum model of phonation

Zhaoyan Zhang,^{a)} Juergen Neubauer, and David A. Berry

The Laryngeal Dynamics Laboratory, Division of Head and Neck Surgery, David Geffen School of Medicine at UCLA, 31-24 Rehabilitation Center, 1000 Veteran Ave., Los Angeles, California 90095-1794

(Received 15 January 2007; revised 23 July 2007; accepted 28 July 2007)

In an investigation of phonation onset, a linear stability analysis was performed on a two-dimensional, aeroelastic, continuum model of phonation. The model consisted of a vocal fold-shaped constriction situated in a rigid pipe coupled to a potential flow which separated at the superior edge of the vocal fold. The vocal fold constriction was modeled as a plane-strain linear elastic layer. The dominant eigenvalues and eigenmodes of the fluid-structure-interaction system were investigated as a function of glottal airflow. To investigate specific aerodynamic mechanisms of phonation onset, individual components of the glottal airflow (e.g., flow-induced stiffness, inertia, and damping) were systematically added to the driving force. The investigations suggested that flow-induced stiffness was the primary mechanism of phonation onset, involving the synchronization of two structural eigenmodes. Only under conditions of negligible structural damping and a restricted set of vocal fold geometries did flow-induced damping become the primary mechanism of phonation onset. However, for moderate to high structural damping and a more generalized set of vocal fold geometries, flow-induced stiffness remained the primary mechanism of phonation onset. © 2007 Acoustical Society of America. [DOI: 10.1121/1.2773949]

PACS number(s): 43.70.Bk, 43.70.Aj [AL]

Pages: 2279–2295

I. INTRODUCTION

Self-sustained oscillation, or flutter, is a general phenomenon which commonly occurs in coupled fluid-structure systems. Vocal fold vibration is one example of this phenomenon. Other examples can be found in biological systems (e.g., the flow-induced instabilities of the blood vessels in arterial stenoses, bronchial airway oscillations during snoring, see [Grotberg and Jensen, 2004](#)) and mechanical systems (e.g., airfoil flutter, see [Dowell and Hall, 2001](#); brass instruments, [Cullen *et al.*, 2000](#)). There have been extensive investigations on the interaction of external flows with compliant plates or membranes (e.g., [Benjamin, 1960](#); [Landahl, 1962](#); [Benjamin, 1963](#); [Pierucci, 1977](#); [Carpenter and Garrad, 1985, 1986](#); [Duncan, 1987](#); [Yeo, 1988, 1992](#); [Lucey and Carpenter, 1993](#); [Yeo *et al.*, 1994](#)). Fluid-structure instabilities due to internal flows through compliant tubes have also been investigated (e.g., [Holmes, 1977](#); [Matsuzaki and Fung, 1977, 1979](#); [Luo and Pedley, 1996](#); [Huang, 2001](#)). Although instabilities in coupled fluid-structure systems can originate from either the fluid or the structure alone, previous investigations have shown that flutter also arises from the coalescence of two eigenmodes (1:1 entrainment) to form a coupled-mode flutter. These two interacting eigenmodes could be either a flow mode coupled to a structural mode (e.g., the vortex-induced vibration, see [Williamson and Govardhan, 2004](#)), or two structural modes (e.g., [Auregan and Depollier, 1995](#); [Cullen *et al.*, 2000](#)).

During normal phonation, it is generally understood that vocal fold vibration involves the excitation of two or more

eigenmodes of the vocal system. For example, early research with the one-mass model ([Flanagan and Landgraf, 1968](#)) showed that self-oscillation of the folds could not occur unless coupled with an acoustic resonance of the vocal tract. However, without a vocal tract, the two-mass model ([Ishizaka and Flanagan, 1972](#)) was able to vibrate through the synchronization of two structural eigenmodes, one with the two masses vibrating in phase with each other, and the other with the two masses vibrating out of phase with each other. The out-of-phase motion created an alternating divergent and convergent glottis, regulating the intraglottal air pressure. The in-phase motion opened and closed the glottal channel, modulating the airflow. The synchronization of empirical modes of vocal fold vibration has also been observed in both theoretical and laboratory models of phonation ([Berry *et al.*, 1994, 2001](#); [Zhang *et al.*, 2006b](#)).

[Titze \(1988\)](#) argued that the propagation of the mucosal wave, or the synchronization of two eigenmodes, facilitated self-oscillation by providing a sufficient, net transfer of energy from the airflow (fluid) to the tissue (structure) to overcome structural damping. However, the linear stability analysis completed by [Titze \(1988\)](#) did not compute the underlying eigenmodes of the two-dimensional vocal fold continuum, but assumed the eigenmodes *a priori*. Also, the temporal phase relationship between the two eigenmodes was imposed, rather than treated as a dynamic variable of the system. Thus, the mechanisms of phonation onset in terms of eigenmode synchronization and the role of glottal aerodynamics in the synchronization process could not be studied.

Using the two-mass model, [Ishizaka and colleagues](#) performed a linear stability analysis to investigate physical mechanisms of phonation onset ([Ishizaka and Matsudaira, 1972](#); [Ishizaka, 1981, 1988](#)). In these investigations, they

^{a)}Author to whom correspondence should be addressed. Electronic mail: zyzhang@ucla.edu

modeled the aerodynamic driving force as a flow-induced stiffness term and showed that the two eigenfrequencies of the two-mass model approximated each other as the flow-induced stiffness was increased (e.g., see pp. 52, 53 of Ishizaka and Matsudaira, 1972; pp. 233, 238 of Ishizaka, 1981). At a threshold of the flow-induced stiffness or subglottal pressure, the two eigenfrequencies synchronized (1:1 entrainment), resulting in phonation onset. Although these studies provided new insight into physical mechanisms of phonation onset, a direct translation of these findings to practical applications has been problematic, perhaps in part because the key model parameters, such as masses and stiffnesses of the coupled oscillators, were immeasurable and difficult to relate to the anatomical structure of the vocal folds (Titze, 1988). Indeed, empirical measurement of the geometric and viscoelastic properties of vocal fold tissues may be more naturally and directly related to the physical properties of continuum models of vocal fold vibration (e.g., Titze *et al.*, 1995; Deverge *et al.*, 2003; Cook and Mongeau, 2007), as opposed to lumped-element models (e.g., Ishizaka and Flanagan, 1972; Steinecke and Herzel, 1995; Story and Titze, 1995; Horacek and Svec, 2002). Furthermore, several investigations have suggested that the eigenfrequency structure of a vocal fold continuum (Berry and Titze, 1996; Cook and Mongeau, 2007) may be much different from the eigenfrequency structure of a lumped-element model (Ishizaka and Matsudaira, 1972; Ishizaka and Flanagan, 1972; Ishizaka, 1981, 1988) resulting in distinct physical mechanisms of phonation onset (Zhang *et al.*, 2006b).

The motivation of the present study is to investigate physical mechanisms of phonation onset in a two-dimensional aeroelastic continuum model of the vocal folds, similar to the investigations of Ishizaka and colleagues for the two-mass model (Ishizaka and Matsudaira, 1972; Ishizaka, 1981, 1988). Similar to Titze (1988), this investigation will apply linear stability analysis to a two-dimensional continuum model of the vocal folds. However, rather than prescribing traveling wave motion and assuming a fixed eigenmode entrainment *a priori*, the present study will utilize a self-oscillating continuum model to investigate the role of glottal aerodynamics in initiating phonation. Using linear plane-strain theory, the vocal fold tissues will be modeled as a two-dimensional continuum, which will be driven by a one-dimensional potential glottal flow with a fixed flow separation location. However, the potential flow utilized here will be more generalized than the one utilized by Ishizaka and colleagues (Ishizaka and Matsudaira, 1972; Ishizaka, 1981), including components not only for flow-induced stiffness, but also flow-induced damping, and flow-induced inertia. Furthermore, in order to investigate specific, aerodynamic mechanisms of phonation onset, the individual components of the glottal airflow will be systematically and separately added to the driving force. That is, initially, only flow-induced stiffness will be considered, as per previous investigations by Ishizaka and colleagues (Ishizaka and Matsudaira, 1972; Ishizaka, 1981, 1988). Next, flow-induced inertia will be added to the driving force, followed by flow-induced damping.

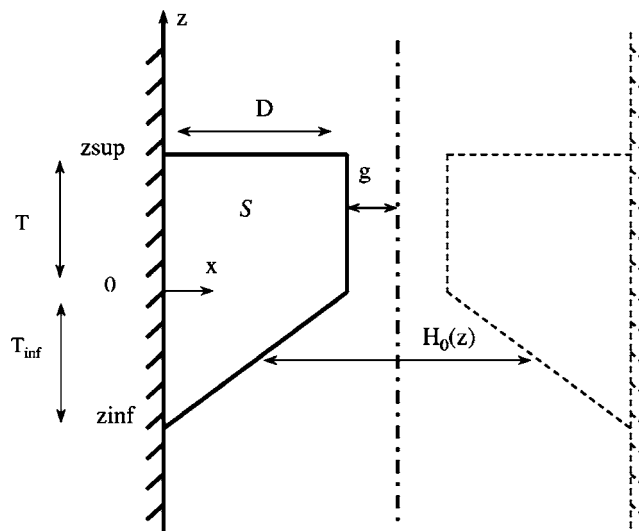


FIG. 1. The two-dimensional vocal fold model and the glottal channel. The flow direction is along the positive z axis. The coupled vocal folds-flow system was assumed to be symmetric about the glottal channel centerline so that only the left half of the system was considered in this study. D is the vocal fold depth in the medial-lateral direction; $T = z_{\text{sup}}$ and $T_{\text{inf}} = -z_{\text{inf}}$ are the thicknesses of the vocal fold in the superior ($z > 0$) and inferior ($z < 0$) sections in the flow direction, respectively; H_0 is the prephonatory glottal channel width; g is the prephonatory glottal half width in the superior part ($z > 0$) of the glottal channel; z_{sup} and z_{inf} are the vertical coordinates of the outlet and inlet of the glottal channel, respectively.

II. MODEL DESCRIPTION

We considered a one-dimensional potential flow through a constriction formed by two symmetric, two-dimensional, isotropic vocal fold-shaped elastic layers. For simplicity, left-right symmetry of the flow and vocal fold vibration about the glottal channel centerline was imposed and therefore only half the system was considered (Fig. 1). A nondimensional formulation was used in this study. The vocal fold thickness T , vocal fold density ρ_{vf} , and the wave velocity of the vocal fold structure $\sqrt{E/\rho_{vf}}$ were used as the reference length, density, and velocity scales, respectively. All variables in the following are in nondimensional forms.

A. Structural model

The vocal folds were modeled as a two-dimensional, isotropic, plane-strain, elastic layer, as shown in Fig. 1. As mentioned above, only one vocal fold was considered. The lateral surface of the vocal fold was fixed to the pipe wall, while the other three sides were fluid-structure-interaction (FSI) boundaries. A linear stress-strain relationship was assumed for the vocal fold material. For a displacement field of the vocal fold structure $[\xi, \eta]$ (the x and z components of the vocal fold displacement, respectively), the corresponding strains and stresses are:

$$\boldsymbol{\varepsilon} = [\varepsilon_x, \varepsilon_z, \gamma_{xz}] = \left[\frac{\partial \xi}{\partial x}, \frac{\partial \eta}{\partial z}, \frac{\partial \xi}{\partial z} + \frac{\partial \eta}{\partial x} \right], \quad (1)$$

$$\boldsymbol{\tau} = [\tau_x, \tau_z, \tau_{xz}] = G\boldsymbol{\varepsilon}, \quad (2)$$

where the stress-strain material matrix G is

$$G = \frac{E(1-\nu)}{(1+\nu)(1-2\nu)} \begin{bmatrix} 1 & \frac{\nu}{1-\nu} & 0 \\ \frac{\nu}{1-\nu} & 1 & 0 \\ 0 & 0 & \frac{1-2\nu}{2(1-\nu)} \end{bmatrix}, \quad (3)$$

where E and ν are the Young's modulus and the Poisson's ratio of the vocal fold material, respectively. The associated kinetic energy V and potential energy U of the vocal fold structure are

$$V = \frac{1}{2} \iint_S (\dot{\xi}^2 + \dot{\eta}^2) \rho_{vf} dS; \quad (4)$$

$$U = \frac{1}{2} \iint_S (\varepsilon_x \tau_x + \varepsilon_z \tau_z + \gamma_{xz} \tau_{xz}) dS,$$

where S is the two-dimensional vocal fold volume, and ρ_{vf} is the vocal fold density.

The governing equations of motion for the vocal fold can be obtained by substituting the above expressions into the Lagrange's equation

$$\frac{d}{dt} \left(\frac{\partial L}{\partial \dot{q}_r} \right) - \frac{\partial L}{\partial q_r} = Q_r, \quad r = 1, 2, \dots, N, \quad (5)$$

where the Lagrangian $L = V - U$, and Q_r is the generalized force acting on the r th generalized coordinate q_r . The generalized coordinates will be defined in Sec. II C.

In Eq. (4), the contribution of the mean stress and deformation fields of the vocal fold due to the mean flow field is not included as part of the potential energy. However, it can be shown that, for a linear stress-strain relationship of the vocal fold material, this contribution is balanced by the mean flow pressure applied to the vocal fold along the interface. Accordingly, the generalized force in our formulation includes only the contribution from the fluctuating flow pressure.

Equation (5) can be reorganized and written in matrix form as

$$M\ddot{q} + Kq = Q, \quad (6)$$

where the mass and stiffness matrices M and K are defined as

$$M_{ij} = \frac{\partial}{\partial \dot{q}_j} \left(\frac{d}{dt} \left(\frac{\partial L}{\partial \dot{q}_i} \right) \right); \quad K_{ij} = \frac{\partial}{\partial q_j} \left(- \frac{\partial L}{\partial q_i} \right). \quad (7)$$

The corresponding generalized force Q is

$$Q_r = - \int_{\ell_{\text{FSI}}} \left(p \frac{\partial \xi}{\partial q_r} n_x + p \frac{\partial \eta}{\partial q_r} n_z \right) d\ell, \quad r = 1, 2, \dots, N, \quad (8)$$

where ℓ_{FSI} denotes the fluid-structure interface with its normal vector n pointing outward from the vocal folds, and p is the flow pressure on the fluid-structure interface. The minus sign in the equation ensures that the force applied by the flow pressure on the vocal fold surface is always directed into the vocal fold structure. To solve the governing equations, an additional equation relating the pressure p and the vocal fold

displacement field $[\xi, \eta]$ is needed, which will be derived in Sec. II B.

A proportional structural damping was assumed for the vocal fold material. Equation (6) can be modified to include structural damping

$$M\ddot{q} + C\dot{q} + Kq = Q, \quad (9)$$

where C is the structural damping matrix. In this study, a constant loss factor σ was used, which relates the mass and damping matrices as follows:

$$C = \sigma\omega M, \quad (10)$$

where ω is the angular frequency.

B. Flow model

The following assumptions were made to simplify the flow through the glottis:

1. The flow was assumed to be a one-dimensional, incompressible, potential flow up to the point of flow separation.
2. The flow separation location was fixed at the superior edge of the vocal folds $z = z_{\text{sup}}$ (Fig. 1). The jet flow discharged into open space with zero pressure recovery ($P_{0,z_{\text{sup}}} = 0$).
3. The flow rate at the vocal fold inlet was constant.

In this study, the mean jet velocity at the flow separation point was used as the major model control parameter. For a given mean jet velocity U_j , the mean velocity distribution U_0 and mean pressure P_0 along the glottal channel were

$$U_0(z) = \frac{2gU_j}{H_0(z)}; \quad P_0(z) = \frac{1}{2}\rho_f U_j^2 \left(1 - \frac{4g^2}{H_0^2} \right), \quad (11)$$

where ρ_f is the air density, g is the mean glottal half width in the superior section ($z > 0$) of the glottal channel (Fig. 1), and H_0 is the mean width of the glottal channel.

The governing equations for the fluctuating flow velocity u and pressure p were obtained by linearization of the one-dimensional continuity equation and Bernoulli's equation around the mean state (U_0, P_0, H_0) [see, e.g., Lighthill, 1978]

$$\frac{\partial h}{\partial t} + \frac{\partial(U_0 h)}{\partial z} + \frac{\partial(u H_0)}{\partial z} = 0, \quad (12)$$

$$\frac{\partial u}{\partial t} + U_0 \frac{\partial u}{\partial z} + u \frac{\partial U_0}{\partial z} + \frac{1}{\rho_f} \frac{\partial p}{\partial z} = 0, \quad (13)$$

where h is the fluctuating component of the glottal channel width. The fluctuating width of the glottal channel is related to the displacement of the vocal fold structure at the fluid-structure interface as

$$h = -2\xi|_{\ell_{\text{FSI}}}. \quad (14)$$

The factor of 2 appears due to the left-right symmetry of the vocal fold vibration. The boundary conditions for the flow are, according to assumptions 2 and 3:

$$u_{z=z_{\text{inf}}} = 0, \quad p_{z=z_{\text{sup}}} = 0, \quad (15)$$

where z_{inf} and z_{sup} are the vertical coordinates of the inlet and outlet of the glottal channel (Fig. 1). Other types of boundary conditions can be also used to model the coupling of the sub- and supraglottal acoustics and the vocal fold vibration. This will be discussed in future work.

The flow pressure within the glottal channel can be obtained by first integrating the linearized continuity Eq. (12), and then the linearized momentum Eq. (13) along the fluid-structure interface. After applying the boundary conditions in Eq. (15), this yields

$$\begin{aligned} \frac{p(z,t)}{\rho_f} &= \int_{z_{\text{sup}}}^z \left(\frac{\partial}{\partial t} + U_0 \frac{\partial}{\partial z} + \frac{\partial U_0}{\partial z} \right) \\ &\times \left[\frac{1}{H_0} \int_{z_{\text{inf}}}^z \left(\frac{\partial}{\partial t} + U_0 \frac{\partial}{\partial z} + \frac{\partial U_0}{\partial z} \right) h dz \right] dz \\ &= p_0(h) + p_1(h_t) + p_2(h_{tt}), \end{aligned} \quad (16)$$

where

$$\begin{aligned} p_0(h) &= \int_{z_{\text{sup}}}^z \left(U_0 \frac{\partial}{\partial z} + \frac{\partial U_0}{\partial z} \right) \left[\frac{1}{H_0} \int_{z_{\text{inf}}}^z \left(U_0 \frac{\partial}{\partial z} + \frac{\partial U_0}{\partial z} \right) h dz \right. \\ &\quad \left. + \frac{\partial U_0}{\partial z} h dz \right] dz = \frac{U_0^2 h}{H_0} - \left(\frac{U_0^2 h}{H_0} \right) \Big|_{z_{\text{sup}}} \\ p_1(h_t) &= \int_{z_{\text{sup}}}^z \left[\frac{1}{H_0} \int_{z_{\text{inf}}}^z \left(U_0 \frac{\partial}{\partial z} + \frac{\partial U_0}{\partial z} \right) h_t dz \right] dz \\ &\quad + \int_{z_{\text{sup}}}^z \left(U_0 \frac{\partial}{\partial z} + \frac{\partial U_0}{\partial z} \right) \left[\frac{1}{H_0} \int_{z_{\text{inf}}}^z h_t dz \right] dz, \quad (17) \\ p_2(h_{tt}) &= \int_{z_{\text{sup}}}^z \frac{1}{H_0} \int_{z_{\text{inf}}}^z h_{tt} dz dz \end{aligned}$$

where the subscripts t and tt denote first and second derivative with respect to time, respectively. The generalized force Q can be then obtained by substitution of Eq. (16) into Eq. (8), and regrouping in the same form as Eq. (16)

$$Q = Q_0 q + Q_1 \dot{q} + Q_2 \ddot{q}, \quad (18)$$

where Q_0 , Q_1 , and Q_2 represent the flow-induced stiffness, flow-induced damping, and flow-induced inertia, respectively.

Equations (16) and (17) show that the fluctuating flow pressure on the FSI surface is composed of three parts, which represent the flow-induced stiffness, damping, and inertia, respectively. The first term, scaling with $\rho_f U_0^2 / H_0$, represents the flow-induced stiffness. This term is generally the most dominant term of the three, especially at large flow velocities. Note that the matrix Q_0 is asymmetric, mainly due to the imposed flow separation at the superior edge (the second term in the equation for $p_0(h)$ which is nonzero). We will show this feature of the flow-induced stiffness matrix to be an essential component of phonation onset. The second term in Eq. (16) is a first-order term in time, which breaks the time reversibility of the equation, and scales with $\rho_f U_0 / H_0$,

corresponding to the flow-induced damping. Under certain conditions, the Q_1 matrix may introduce negative damping and be destabilizing, as discussed in Sec. III D. The last term, scaling with ρ_f / H_0 , represents the added-mass effect, and is always present even for zero flow velocity.

C. Ritz method

In this study, the Ritz method was used to solve Eq. (9). The displacement field of the vocal fold structure was approximated as

$$\xi(x,z,t) = \sum_{i=1}^I \sum_{k=0}^K A_{ik}(t) x^i z^k; \quad \eta(x,z,t) = \sum_{i=1}^I \sum_{k=0}^K B_{ik}(t) x^i z^k. \quad (19)$$

The generalized coordinates were therefore defined as

$$[q_r] = [A_{10}, A_{11}, \dots, A_{IK}, B_{10}, \dots, B_{IK}]_{N=2 \times I \times (K+1)}. \quad (20)$$

In terms of the generalized coordinates, the fluctuating glottal width was

$$\begin{aligned} h &= -2\xi \Big|_{\ell_{\text{FSI}}} = -2 \sum_{i=1}^I \sum_{k=0}^K A_{ik}(t) x^i z^k \Big|_{\ell_{\text{FSI}}} \\ &= -2 \sum_{i=1}^I \sum_{k=0}^K A_{ik}(t) f(z)^i z^k, \end{aligned} \quad (21)$$

where $x=f(z)$ describes the prephonatory fluid-structure interface up to the point of flow separation.

D. Linear stability analysis

Substitution of Eq. (18) into Eq. (9) yields

$$(M - Q_2) \ddot{q} + (C - Q_1) \dot{q} + (K - Q_0) q = 0. \quad (22)$$

The equation can be written as

$$\begin{aligned} \begin{bmatrix} \dot{q} \\ \ddot{q} \end{bmatrix} &= \begin{bmatrix} 0 & I \\ -(M - Q_2)^{-1}(K - Q_0) & -(M - Q_2)^{-1}(C - Q_1) \end{bmatrix} \\ &\times \begin{bmatrix} q \\ \dot{q} \end{bmatrix}, \end{aligned} \quad (23)$$

where I is the identity matrix.

Assuming $q = q_0 e^{st}$, the equation is solved as an eigenvalue problem for the eigenvalues s and eigenmodes, q_0 . Each eigenvalue corresponds to an eigenmode of the coupled fluid-structure system. To differentiate these eigenmodes from the *in vacuo* modes of the vocal fold structure, they will be referred to as FSI eigenmodes throughout the rest of the paper. The real and imaginary parts of the eigenvalue correspond to the growth rate and the oscillation frequency of the eigenmode, respectively. A positive growth rate indicates that the amplitude will increase with time, indicative of a linearly unstable eigenmode. The mean state of the coupled system is linearly stable if all eigenvalues have negative growth rates. Thus, phonation onset for a particular vocal fold configuration can be studied by solving the eigenvalue problem over a range of subglottal pressures. The phonation threshold pressure would be the subglottal pressure at which the real part

of one eigenvalue first becomes positive. The vibration pattern of the vocal folds at onset would then be given by the corresponding eigenvector.

Note that the mean state (U_0, P_0, H_0) of the coupled system, around which the system equations are linearized, is a function of subglottal pressure. Therefore, for a given subglottal pressure, a nonlinear steady-state problem has to be solved to determine the mean equilibrium state of the coupled system before conducting linear stability analysis around this mean state. For simplicity, the step was skipped in this study and the linear stability analysis was performed on a given mean deformed vocal fold geometry. The mean equilibrium state of the vocal fold was assumed to remain unchanged as the subglottal pressure was increased. With this simplification, the analysis in this study focused on the linear stability of a given pre-phonatory vocal fold geometry.

Note that our model formulation is based on linear theory and therefore does not apply beyond onset. To study the behavior of the system beyond onset, the original nonlinear equations would need to be solved (see, e.g., Holmes, 1977; Guckenheimer and Holmes, 1983).

E. FSI mode decomposition using PCA

Generally the eigenvectors of Eq. (23) are complex. Together with the time dependent factor, e^{st} , a complex eigenvector describes a wave motion along the vocal fold surface, i.e., the vibration of the vocal fold along the FSI interface has no fixed nodal lines. This wave motion can be decomposed into two standing wave components. For the convenience of physical interpretation and direct comparison between different cases, it is desirable to find a consistent decomposition method that can decompose each of the FSI eigenmodes into two spatially and temporally orthogonal components. Using principal components analysis (PCA), each FSI eigenmode was decomposed into two spatially and temporally orthogonal components: a FSI-1 mode and a FSI-2 mode. By definition, the FSI-1 mode captured the largest percentage of the total energy of the original FSI eigenmode. PCA gives an optimal and consistent decomposition: the strongest mode (the FSI-1 mode) obtained using PCA captures more energy than that of any other decomposition (Holmes *et al.*, 1996). The use of PCA would also make it possible to compare the results of this study to previous experimental work in which empirical eigenfunctions of the vocal fold medial surface dynamics were calculated.

For a complex eigenvector q , a matrix could be formed by combining the real and imaginary parts of the eigenvector q

$$X = [\text{Re}(q), \text{Im}(q)] \quad (24)$$

from which a covariance matrix was calculated

$$\text{Cov}(X) = X^T M X, \quad (25)$$

where the superscript T denotes the transpose of the matrix. Eigenvalue analysis of the covariance matrix yields two PCA eigenvalues (λ_1, λ_2) and eigenvectors (Ψ_1, Ψ_2) . The two eigenvectors provide an orthonormal basis consisting of two vectors whose relative energy weights are given by the rela-

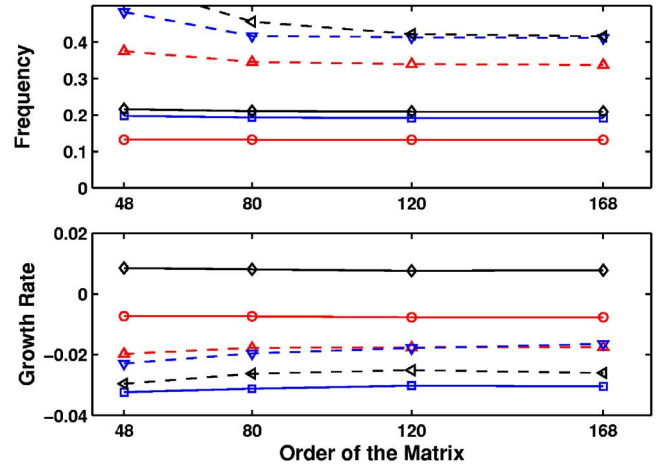


FIG. 2. (Color online) The frequencies and growth rates of the first six eigenvalues (\circ : first; \square : second; \diamond : third; \triangle : fourth; ∇ : fifth; \triangleleft : sixth) of Eq. (23) as a function of the matrix orders of Eq. (23). The values of model parameters specified in Eq. (28) were used, with a loss factor of 0.1. The order of the matrices in Eq. (23) equals $4 \times I \times (K+1)$. $I=K=3, 4, 5$, and 6 for the four sets of data shown.

tive values of the corresponding eigenvalues. The original eigenvector q can then be projected onto the two orthonormal vectors, giving the final form of the FSI-1 and FSI-2 modes

$$q_{\text{FSI-1}} = \langle q, \Psi_1 \rangle \Psi_1, \quad q_{\text{FSI-2}} = \langle q, \Psi_2 \rangle \Psi_2, \quad (26)$$

where the angular bracket denotes a vector dot product, which is defined as

$$\langle v_1, v_2 \rangle = v_1^* M v_2, \quad (27)$$

where the superscript $*$ denotes complex conjugate, the superscript T denotes transpose, and M is the mass matrix of the vocal fold structure. With this definition, the orthogonality of two vectors is based on the entire vocal fold volume rather than just the medial surface of the vocal folds as implemented in previous laboratory experiments (Berry *et al.*, 2001, 2006).

F. Numerical convergence

Figure 2 shows the eigenvalues of Eq. (23) as a function of the order of the matrices in Eq. (23). Values of the model parameters in Eq. (28) were used, together with a loss factor of 0.1 and a mean jet velocity of 6. For given values of (I, K) for the orders of the polynomials used in Eq. (19), the order of matrices in Eq. (23) equals $4I(K+1)$. It can be seen that convergence was reached for the first four lowest eigenvalues when the order of the matrices was 80 (or above), which corresponded to $I=K=4$ in Eq. (19). In this study, the results presented below were all obtained for this setting. Note that, at this setting, convergence was not reached for higher-frequency eigenvalues. Because higher-frequency eigenmodes tend to dampen out quickly in most real life applications, we focused exclusively on the first four eigenmodes in this study.

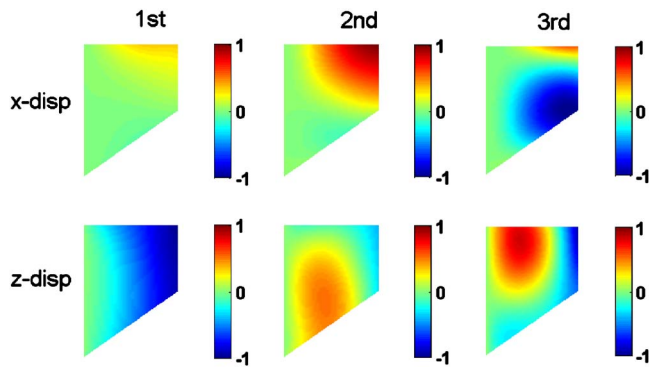


FIG. 3. (Color online) The first three *in vacuo* eigenmodes of the vocal fold, for model parameters specified in Eq. (28). The first and second rows show the x component (medial-lateral direction) and z component (inferior-superior direction) of the eigenmodes, respectively.

III. RESULTS

This section is organized as follows. Results will first be presented for the case when all three flow terms are excluded from the system Eq. (22) (Sec. III A), which is equivalent to the *in vacuo* condition which was studied in previous investigations (Berry and Titze, 1996; Cook and Mongeau, 2007). Next, the flow-induced stiffness (Sec. III B), inertial (Sec. III C), and damping (Sec. III D) terms will be added sequentially to the equation. Using this procedure, the effects of these three individual terms will be investigated systematically. Through an analysis of the energy flow and the evolution of the eigenvalues, we will show that the flow-induced stiffness was the primary aerodynamic mechanism of phonation onset, involving the excitation and synchronization of two structural eigenmodes. Only under conditions of negligible structural damping and a restricted set of vocal fold geometries did flow-induced damping become the primary mechanism of phonation onset. At moderate and high structural damping, flow-induced stiffness remained the primary aerodynamic mechanism of phonation onset.

For the results presented below, unless otherwise stated, the following nondimensional values for the model parameters were used (see definition in Fig. 1):

$$D = 1.4, g = 0.0714, T_{\text{inf}} = 1, \rho_f = 0.0012, \nu = 0.47, \quad (28)$$

which corresponded to the following physical values (the first four are the scaling variables):

$$T = 7 \text{ mm}, \rho_{vf} = 1030 \text{ kg/m}^3, E = 3 \text{ kPa},$$

$$U_{\text{scaling}} = 1.7 \text{ m/s}, D = 10 \text{ mm}, g = 0.5 \text{ mm}, \quad (29)$$

$$T_{\text{inf}} = 7 \text{ mm}, \rho_f = 1.2 \text{ kg/m}^3, \nu = 0.47.$$

A. *In vacuo* eigenmodes of the vocal fold

The *in vacuo* eigenmodes of the vocal fold can be obtained by solving Eq. (6) with the right hand side of the equation set to zero. Since no first-order term in time exists in Eq. (6) and both the mass and stiffness matrices are positive definite, the eigenspectrum in this case lies on the imaginary axis, i.e., the growth rates of all eigenvalues are zero.

Figure 3 shows the first three *in vacuo* eigenmodes of the vocal fold. The corresponding eigenfrequencies were 0.102, 0.214, and 0.239 (or 25, 52.2, and 58.2 Hz in physical units for model parameters given in Eq. (29)). The first *in vacuo* eigenmode captured a dominant in-phase vertical motion along the vocal fold medial surface with a weak lateral motion near the superior edge. The second eigenmode captured a dominant in-phase lateral motion along the medial surface. Note that the maximum lateral displacement of the vocal fold along the medial surface occurred at the superior edge. The third eigenmode, in contrast to the first two modes, captured an out-of-phase lateral motion along the vocal fold medial surface. Note that, for the third eigenmode, a nodal line of the lateral displacement existed near the superior edge of the vocal fold. These major features of the first three *in vacuo* eigenmodes of the vocal fold structure are consistent with previous studies (Titze and Strong, 1975; Berry and Titze, 1996).

B. Mechanisms of phonation onset: Flow-induced stiffness

Next we added the flow terms, the matrix Q (Eq. (18)), to the system. For the case of phonation, in which airflow interacts with the vocal fold structure, the density ratio between the flow and structure is very small ($\rho_f \sim 10^{-3}$, Eq. (28)). Therefore, for not so large jet velocities, the flow pressure term Q is generally small compared to the structural mass and stiffness terms in Eq. (22). In particular, the last two terms (Q_1 and Q_2) in Eq. (18) can be neglected and only the flow stiffness term, Q_0 , is retained. In the following, we show first the results obtained when only the flow stiffness term was included. This condition is analogous to the linear stability analysis of Ishizaka and colleagues for the two-mass model in which only the flow-induced stiffness was considered (e.g., see pp. 52 and 53 of Ishizaka and Matsudaira, 1972; pp. 233, 238 of Ishizaka, 1981). The other terms in Eq. (16) will be included in subsequent sections of this paper.

1. Eigenmode synchronization

With only the Q_0 term included and structural damping neglected, Eq. (22) becomes

$$M\ddot{q} + (K - Q_0)q = 0. \quad (30)$$

Equation (30) represents a competition between two mechanisms. One is the stabilizing structural restorative forces, the structural stiffness K , and the other is the destabilizing mechanism due to the flow-induced stiffness, Q_0 . The solution of Eq. (30) depends on the structure of the flow-induced matrix Q_0 . For a symmetric Q_0 matrix, the system loses stability to a static divergence instability (zero frequency instability). This occurs when the flow stiffness term exceeds the structural stiffness term. However, for an asymmetric Q_0 matrix (e.g., due to a nonconservative system), the asymmetric nondiagonal elements in matrix Q_0 induce a cross-mode coupling effect, causing two neighboring eigenvalues to approximate each other and eventually collide. When this coupling effect is strong, the system loses stability to a coupled-mode flutter instability (Weaver, 1974; Holmes, 1977; Auregan and

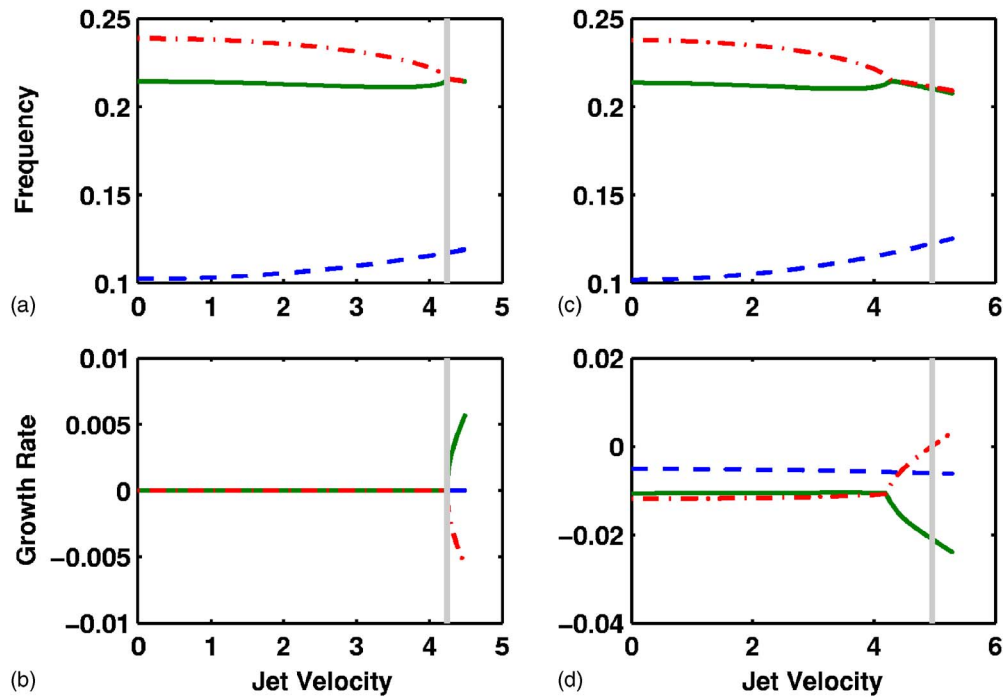


FIG. 4. (Color online) The frequencies and growth rates of the first three eigenvalues (---: first; —: second; -.-: third) of the coupled fluid-structure system as a function of the jet velocity. The vertical line indicates the point of onset. Model parameters specified in Eq. (28) were used. Only the flow stiffness term Q_0 of the three flow-induced terms was included in Eq. (22). Figures 4(a) and 4(b): $\sigma=0$, the corresponding eigenvalue movement in the complex half plane is shown in Fig. 5(a); Figs. 4(c) and 4(d): $\sigma=0.1$, the corresponding eigenvalue movement in the complex half plane is shown in Fig. 5(b).

Depollier, 1995; Cullen *et al.*, 2000), as further illustrated below.

Figures 4(a) and 4(b) show the first three eigenfrequencies of Eq. (30) and their associated growth rates as a function of jet velocity. At zero velocity, Eq. (30) reduces to Eq. (6) with the eigenvalues corresponding to the *in vacuo* eigenvalues of the vocal fold. As the jet velocity increased, the second and third eigenvalues approached each other in frequency while the growth rates for all remained zero. At a threshold value of the jet velocity (phonation onset), the second and third eigenfrequencies merged into one frequency, while at the same time one growth rate became positive and the other negative. Figure 5(a) shows the movement of the second and third eigenvalues in the complex half plane. Note that, although eigenvalues always come in complex conjugate pairs, only the eigenvalues with positive imaginary part are shown in the complex half plane in Fig. 5. Before onset, all the eigenvalues lay on the imaginary axis. As the flow velocity increased, the second and third eigenvalues, mainly the third eigenvalue, moved towards each other due to the coupling effect of the flow. At onset, the two eigenvalues collided and split into two eigenvalues with the same frequency but with nonzero growth rates of opposite sign. Therefore, in this case, onset occurred via a 1:1 resonance mechanism (Guckenheimer and Holmes, 1983) of the second and third eigenvalues.

Note that the asymmetric nature of the matrix Q_0 in our model was mainly due to the imposed flow separation (see Eqs. (8) and (17)). For a potential flow formulation without flow separation, the matrix Q_0 would be nearly symmetric, and Eq. (30) would lose stability first to a static divergence of the first eigenmode, rather than to a coupled-mode flutter

instability. In fact, coupled-mode flutter is facilitated by any factor or mechanism which makes the matrix Q_0 asymmetric. For example, our simulations showed that coupled-mode flutter also occurred first for Eq. (30) for sufficiently large viscous flow resistance but without flow separation.

The structural restorative force in the vocal folds scales with $\omega_0^2 \xi$, where ω_0 is the *in vacuo* eigenfrequency. The flow-induced stiffness term, and therefore the coupling strength, roughly scales with $\rho_f U_j^2 \xi / g$. Therefore, a balance between the structural stiffness and the flow-induced stiffness yields the following expressions or proportionalities for the jet velocity and subglottal pressure at onset:

$$U_j \sim \omega_0 \sqrt{\frac{g}{\rho_f}}; \quad P_{0,\text{in}} \sim \omega_0^2 g. \quad (31)$$

The *in vacuo* eigenfrequency ω_0 is a function of the material properties of the vocal folds, vocal fold geometry, and boundary conditions (Berry and Titze, 1996; Cook and Mongeau, 2007).

2. Vocal fold vibration at onset

The eigenmode with the largest growth rate, or the critical eigenmode, was analyzed to investigate vocal fold vibration characteristics at onset. The phonation frequency, or the imaginary part of the eigenvalue of the critical eigenmode, was in between the second and third *in vacuo* eigenfrequencies, slightly closer to the second *in vacuo* eigenfrequency, as shown in Fig. 4(a). The corresponding complex eigenvector was decomposed into two spatially and temporally orthogonal FSI modes, as described in Sec. II E. The vibration pattern of the vocal fold for each FSI mode can be obtained by

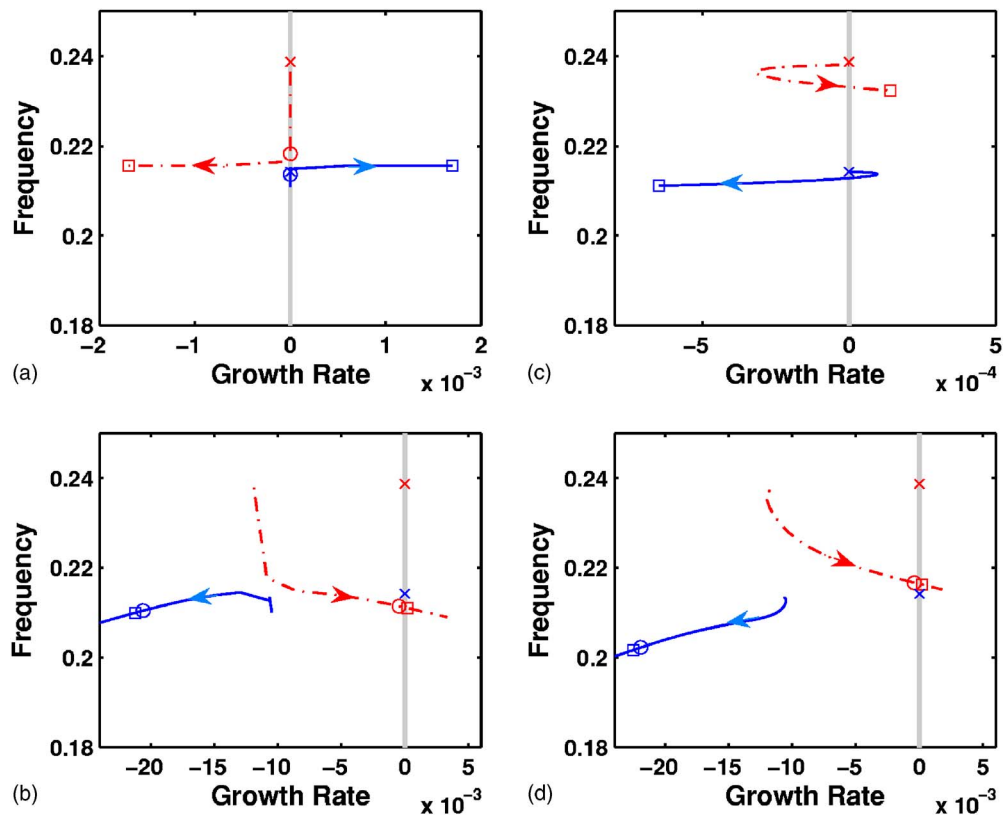


FIG. 5. (Color online) Movement of the second and third eigenvalues in half complex plane. Model parameters specified in Eq. (28) were used. (a) with only the flow stiffness term Q_0 of the three flow-induced terms included, $\sigma=0$; (b) with only the flow stiffness term Q_0 of the three flow-induced terms included, $\sigma=0.1$; (c) with all three flow-induced terms included, $\sigma=0$; (d) with all three flow-induced terms included, $\sigma=0.1$; \times : *in vacuo* eigenvalues; \circ : eigenvalues before onset; \square : eigenvalues after onset. The arrows indicate the direction of the movement of the eigenvalues as the jet velocity increases. The vertical lines indicate the imaginary axis.

substituting the corresponding eigenvector into Eq. (19), and is shown in Fig. 6.

The dominant FSI mode, FSI-1, captured an out-of-phase lateral motion and an equally strong in-phase vertical motion along the medial surface. The second FSI mode, FSI-2, captured a dominant in-phase lateral motion and a relatively weak vertical motion along the medial surface. Neither of the FSI modes closely resembled the *in vacuo*

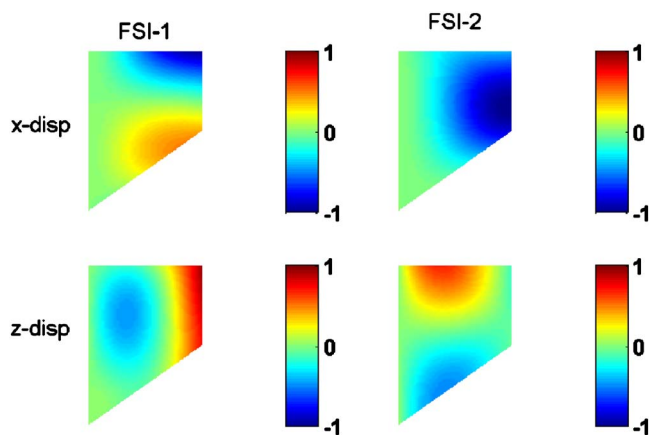


FIG. 6. (Color online) Vibration patterns of the FSI-1 (left) and FSI-2 (right) modes at onset for case shown in Fig. 5(a) ($Q=Q_0q$, model parameters given by Eq. (28), $\sigma=0$). The first and second rows show the x component (medial-lateral direction) and z component (inferior-superior direction) of the eigenmodes, respectively.

eigenmodes of the vocal fold. In fact, the FSI-1 and FSI-2 were to some degree similar to the third and second *in vacuo* eigenmodes with the vibration pattern (within the entire vocal fold volume) shifted inferiorly, respectively. For example, in the FSI-1 mode, a horizontal (medial-lateral) nodal line of the lateral displacement (x component) of the vocal fold existed around the center of the superior section ($z > 0$) of vocal fold in the inferior-superior direction, as compared to the nodal line near the superior edge for the third *in vacuo* eigenmode of the vocal fold (Fig. 3). In the FSI-2 mode, the maximum lateral displacement along the medial surface occurred around the center of the superior section of the vocal fold surface, shifted inferiorly from its location at the superior edge for the second *in vacuo* eigenmode. To quantify the similarity between the FSI modes and the *in vacuo* modes, correlations (vector dot product) between the two FSI modes and the *in vacuo* eigenmodes were calculated based on Eq. (27). The correlations between the FSI-1 mode and the first three *in vacuo* eigenmodes were 31.3%, 69.1%, and 65.1%, respectively. For the FSI-2 mode, its correlations with the first three *in vacuo* eigenmodes were 13.5%, 64.75%, and 75.0%, respectively. The correlation between the two FSI modes and higher-order *in vacuo* eigenmodes was nearly zero so that both FSI modes could be reproduced by a combination of the first three *in vacuo* eigenmodes with an accuracy above 99%.

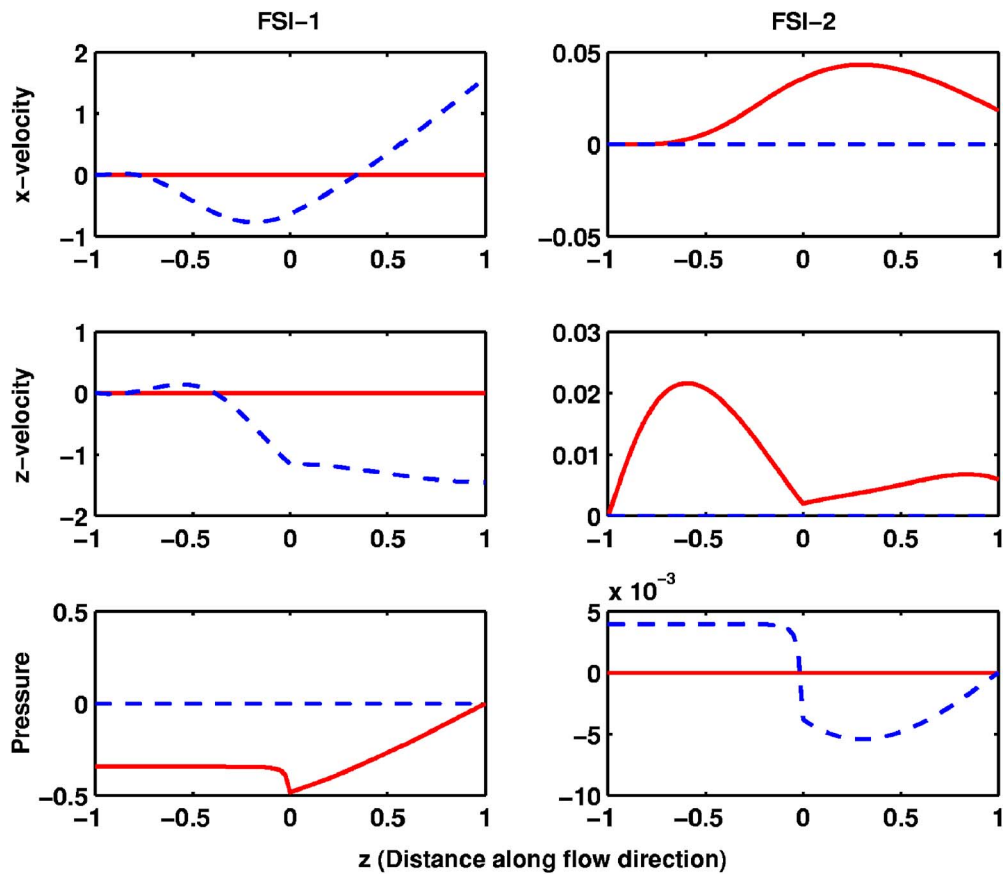


FIG. 7. (Color online) The vocal fold velocity in medial-lateral and inferior-superior directions and the flow pressure along the vocal fold surface corresponding to the FSI-1 and FSI-2 modes as shown in Fig. (6). —: real part; - -: imaginary part.

At onset, the relative energy weights (λ_1, λ_2) of the FSI-1 and FSI-2 modes were 99.9% and 0.1%, respectively, which indicates that the vocal fold vibration was essentially a single-mode, standing wave motion rather than a traveling wave motion. Ideally, at the exact point of onset, all the eigenvalues of Eq. (30) are still on the imaginary axis, including the colliding pair. The eigenvectors corresponding to the colliding pair of eigenvalues would be real. In this case (without structural damping), the space spanned by the two FSI modes is reduced to a one-dimensional space, i.e., a single mode rather than a traveling wave motion. The relative energy weights of the two FSI modes would be 100% and 0%, representing a single-mode vibration pattern. Our numerical analysis did not catch the exact onset point so that the relative weights deviated from the exact theoretical values. When structural damping is included, as shown later in Sec. III B 4, the onset would be delayed until after the eigenvalue collision. The eigenvector of the critical eigenmode would therefore be complex, describing a traveling wave as generated by the superposition of two FSI modes. In the complex full plane, this eigenmode corresponded to a complex conjugate pair of eigenvalues, with a complex conjugate pair of eigenvectors. The space spanned by the two FSI modes is therefore two dimensional. The weight of the FSI-1 mode would decrease from 100% and two FSI modes would then be needed to describe the vocal fold vibration. With

increasing structural damping, the two eigenvectors will further deviate away from each other, leading to more comparable weights for the two FSI modes (Sec. III B 4).

3. Energy transfer

Figure 7 shows the vocal fold velocity and pressure distribution along the medial surface of the vocal fold for the two FSI modes slightly above onset. For both modes, the pressure was 90° out of phase with the velocity (one was nearly pure real and the other was nearly pure imaginary) except for a very small in-phase component. The first FSI mode, FSI-1, captured an out-of-phase lateral motion along the medial surface, creating an alternating convergent/divergent glottis near the superior part of the glottal channel ($0 < z < 1$). Due to the zero pressure boundary condition at the superior edge of the glottal channel, this motion created an alternating in-phase increase/decrease in the pressure along the glottal channel. On the other hand, the FSI-2 mode induced an out-of-phase pressure distribution along the glottal channel.

From the distribution of the vocal fold velocity along the medial surface and the pressure along the glottal channel, the energy flow from the fluid into the structure was calculated as

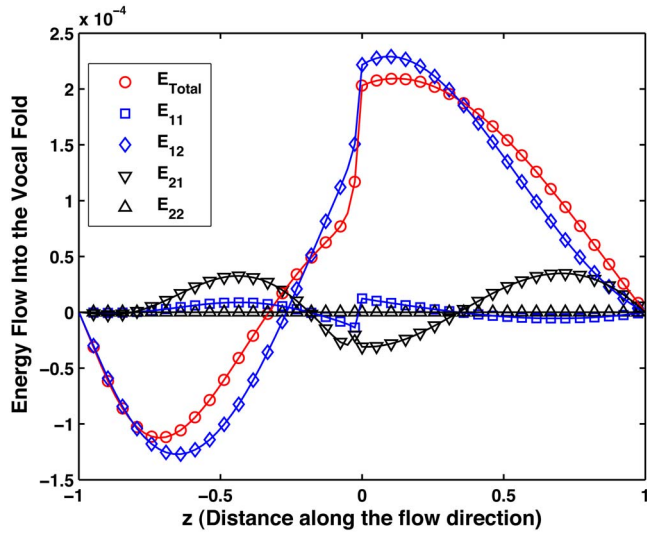


FIG. 8. (Color online) Distribution of total energy flow into the vocal fold along the vocal fold surface and its decomposition into contributions of two self-mode and two cross-mode interaction terms for the case shown in Fig. 5(a) (model parameters given in Eq. (28), $Q=Q_{0g}$, and $\sigma=0$, slightly above onset). See Eqs. (32) and (33) for the definition of different energy terms.

$$E_{total} = -\frac{1}{2} \operatorname{Re}(p\dot{\xi}^* n_x + p\dot{\eta}^* n_z) \Big|_{\ell_{FSI}} = E_{11} + E_{12} + E_{21} + E_{22}, \quad (32)$$

where

$$\begin{aligned} E_{11} &= -\frac{1}{2} \operatorname{Re}(p_{f_{si-1}} \dot{\xi}_{f_{si-1}}^* n_x + p_{f_{si-1}} \dot{\eta}_{f_{si-1}}^* n_z) \Big|_{\ell_{FSI}}, \\ E_{12} &= -\frac{1}{2} \operatorname{Re}(p_{f_{si-1}} \dot{\xi}_{f_{si-2}}^* n_x + p_{f_{si-1}} \dot{\eta}_{f_{si-2}}^* n_z) \Big|_{\ell_{FSI}}, \\ E_{21} &= -\frac{1}{2} \operatorname{Re}(p_{f_{si-2}} \dot{\xi}_{f_{si-1}}^* n_x + p_{f_{si-2}} \dot{\eta}_{f_{si-1}}^* n_z) \Big|_{\ell_{FSI}}, \\ E_{22} &= -\frac{1}{2} \operatorname{Re}(p_{f_{si-2}} \dot{\xi}_{f_{si-2}}^* n_x + p_{f_{si-2}} \dot{\eta}_{f_{si-2}}^* n_z) \Big|_{\ell_{FSI}}. \end{aligned} \quad (33)$$

In Eq. (32), the total energy flow is decomposed into two self-mode interaction terms and two cross-mode interaction terms. Figure 8 shows the distribution of the total energy flow along the glottal channel. In this case, energy flow was negative along the inferior part of the glottal channel ($z < 0$), indicating that energy was transferred from the structure to the fluid. In the superior part of the glottal channel ($z > 0$), energy flow was reversed and energy was transferred from the fluid into the structure at a slightly greater rate than that at which energy was extracted from the inferior vocal fold structure. In total a net positive energy transfer was established from the fluid into the vocal fold structure. Figure 8 also shows the individual contributions of the self-mode and cross-mode interaction between the two FSI modes. The contributions of the two self-mode interaction terms were small, as expected for a pressure field nearly 90° out of phase with the velocity. Of the two cross-mode terms,

E_{12} was the most dominant term, which represented the interaction between the pressure field induced by the out-of-phase FSI-1 mode and the velocity field induced by the in-phase FSI-2 mode. Integrated along the glottal channel, the four energy terms ($E_{11}, E_{12}, E_{21}, E_{22}$) contributed 1.14%, 83.71%, 15.14%, and 0.01% to the total energy flow, respectively.

The above analysis further clarified the onset mechanism from the point of view of energy transfer. As discussed in Sec. III B 2, a major difference between the eigenvalues before and after onset is that the complex eigenvalues after onset resulted in complex eigenvectors, describing a wave motion or the synchronization of two FSI modes at precisely the same frequency. Without this synchronization, the energy flow would be zero as the pressure induced by the same mode would be always 90° out of phase with the vocal fold velocity. It is only because of the synchronization of two modes that the total pressure field had an in-phase component with the total vocal fold velocity field (Fig. 7), no matter how small the FSI-2 mode was in amplitude compared to the FSI-1 mode. In particular, the most effective energy transfer contribution came from the interaction between the pressure field of the FSI-1 mode (capturing an out-of-phase lateral motion) with the velocity field of the FSI-2 mode (capturing an in-phase lateral motion). This is consistent with previous understanding (Ishizaka, 1981, 1988; Titze, 1988; Berry and Titze, 1996) that two eigenmodes of the vocal fold vibration “entrained” to create favorable aerodynamic conditions for phonation: one eigenmode shapes the top of the glottal airway to be alternately convergent/divergent during one glottal oscillation cycle, therefore modulating the intraglottal pressure, while the other eigenmode governs the net lateral tissue velocity and modulates the flow velocity. The two eigenmodes interacted to facilitate energy transfer from the airflow to the vocal fold tissue, as shown in Fig. 8.

Since no damping terms (either structural or flow induced) were included in the present example, the energy flow at onset must be identically zero rather than nonzero, as in the above energy analysis. However, since the eigenvalue problem (Eq. (30)) was solved numerically in this study, the exact point of onset was not captured. Therefore, the onset jet velocity as identified in this study was always slightly larger. While our model formulation no longer applies after onset, it will be shown below that the general conclusions (the vibration patterns of the two FSI modes and energy transfer) made in this subsection still hold for cases with nonzero structural damping, in which a nonzero energy flow was present to balance the structural dissipation.

4. Effects of structural damping

Inclusion of structural damping shifted the eigenspectrum of the system to the left in the complex half plane, as shown in Fig. 5(b) for the same set of model parameters but with a loss factor of $\sigma=0.1$. Figures 4(c) and 4(d) show the corresponding frequency and growth rate of the first three eigenmodes. The physical mechanism of onset remained the same: two eigenvalues approached each other and then separated again, one of which eventually crossed the imaginary axis as the jet velocity continued to increase, causing the

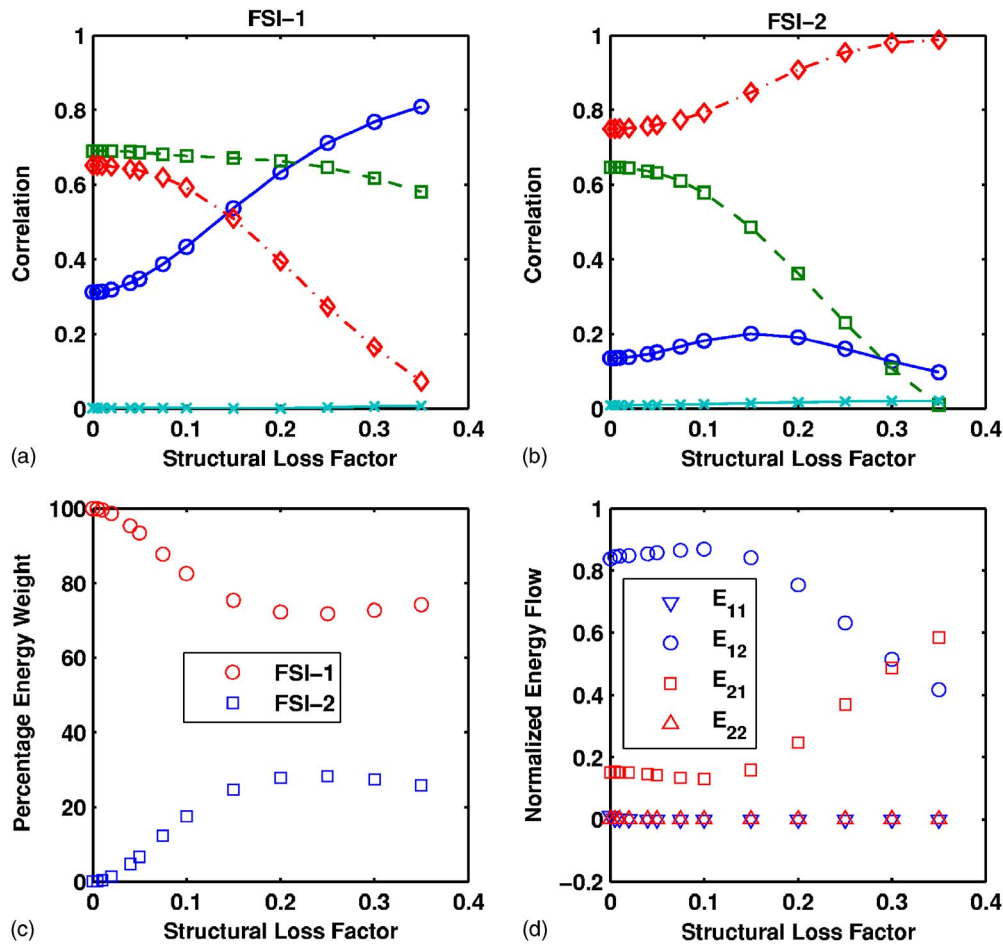


FIG. 9. (Color online) Correlation between the FSI-1 mode (a) and FSI-2 mode (b) and the first four *in vacuo* eigenmodes (\circ : first; \square : second; \diamond : third; \times : fourth *in vacuo* eigenmodes), relative energy weights of the two FSI modes (c) and normalized contributions to the total energy flow by individual interaction terms (d) as a function of the structural loss factor. Model parameters were given in Eq. (28), $Q=Q_0q$.

corresponding eigenmode to become linearly unstable. However, in contrast to the case of Fig. 5(a), the two eigenvalues in Fig. 5(b) approached but never actually collided with each other. Note the similarity between Figs. 4(c) and 4(d) in this paper and Fig. 5 of (Ishizaka, 1981, p. 238). Using two different computational models, both figures have apparently captured the same physical mechanism.

Figure 9 shows the correlations between the two FSI modes and the first four *in vacuo* eigenmodes as a function of the loss factor. Both FSI modes were a mixture of mainly the first three *in vacuo* eigenmodes of the vocal folds, with negligible correlations with the fourth and higher *in vacuo* eigenmodes (Figs. 9(a) and 9(b)). For small and moderate structural damping, the vocal fold vibration patterns captured by the two FSI modes were qualitatively similar to the case without structural damping. The FSI-1 mode captured an out-of-phase lateral motion, with a nodal line along the center of the medial surface, and an in-phase vertical motion along the medial surface of the vocal fold. The FSI-2 mode captured a dominant, in-phase lateral motion with a weak, in-phase vertical motion along the vocal fold medial surface. As the loss factor increased, the correlation with the third *in vacuo* eigenmode slightly decreased (increased) for the FSI-1 (FSI-2) mode. For the FSI-1 mode, this caused the nodal line of the lateral displacement to continuously shift inferiorly.

For the FSI-2 mode, this caused the location of the maximum lateral displacement along the medial surface to shift inferiorly. There was a threshold value of the structural loss factor (around $\sigma=0.25$) at which the vibration patterns captured by the two FSI modes became qualitatively similar. Beyond this threshold, a switchover occurred in the vibration patterns captured by the two FSI modes. The FSI-1 mode now captured an in-phase lateral motion while the FSI-2 mode captured an out-of-phase lateral motion.

Figure 10 shows the onset jet velocity and onset frequency as a function of the loss factor, for model parameters specified by Eq. (28). The onset frequency in this case slightly decreased with the loss factor. With structural damping included, more energy transfer was needed to overcome the structural dissipation, delaying onset to a higher value of the jet velocity. This additional energy transfer was achieved by the increasing relative weight of the FSI-2 mode with the loss factor (Fig. 9(c)). With more comparable weights of the two FSI modes, the total flow pressure became more in phase with the vocal fold velocity, which increased the energy transfer efficiency and allowed more energy transfer to overcome structural dissipation.

The energy transfer mechanisms remained similar to the case without structural damping. Except for ranges of loss factors in which the two FSI modes became similar, the ma-

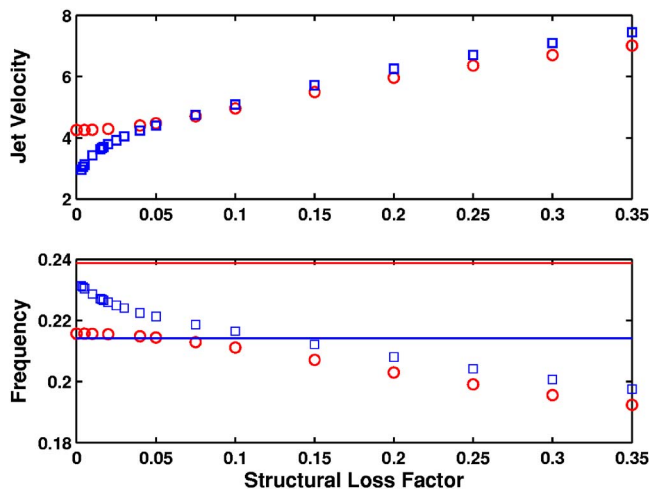


FIG. 10. (Color online) Onset jet velocity (top) and frequency (bottom) as a function of the structural loss factor, for model parameters given in Eq. (28). \circ : $Q=Q_0q$; \square : $Q=Q_2\dot{q}+Q_1\dot{q}+Q_0q$. The two horizontal lines indicate the second and third *in vacuo* eigenfrequencies.

major contribution of energy flow still came from the interaction between the pressure field induced by the out-of-phase FSI mode and the vocal fold motion of the in-phase FSI mode (Fig. 9(d)). The other cross-mode interaction term also positively contributed to the total energy flow. The contributions from the same-mode interaction were negligible.

C. Effects of flow-induced inertia

As discussed in Sec. II B, the flow-induced inertia term, p_2 , is the weakest term of the three parts in Eq. (16), due to the small density ratio between air and the vocal fold. When included, the eigenspectrum remained nearly the same as when it was excluded, with only slight changes in the frequencies. The difference was nearly unnoticeable except for very small glottal half widths, which would change the relative weight of the flow-induced inertia term with respect to the structural mass term (Eq. (17)).

D. Effects of flow-induced damping

1. Destabilization effects

The flow-induced damping term, p_1 , is a first-order term in time. It breaks the time reversal symmetry of Eq. (30), and, depending on the structure of the matrix Q_1 , may directly destabilize the coupled fluid-structure system. Figures 11(a) and 11(b) show the first three eigenvalues as a function of increasing jet velocity. The model parameters were the same as in Sec. III A. (Eq. (28), and zero structural damping), but with all three flow terms, Q_0 , Q_1 , and Q_2 included in Eq. (22). The corresponding movement of the second and third eigenvalues in the complex half plane is shown in Fig. 5(c). Unexpectedly we found that the second eigenmode immediately became unstable when a nonzero flow was applied, while at the same time the first and third eigenmodes were stabilized. In other words, the onset jet velocity was infinitesimally small.

This seemingly unlikely result was due to the presence of an irreversible perturbation (the flow-induced damping term) in an otherwise reversible system. The irreversible per-

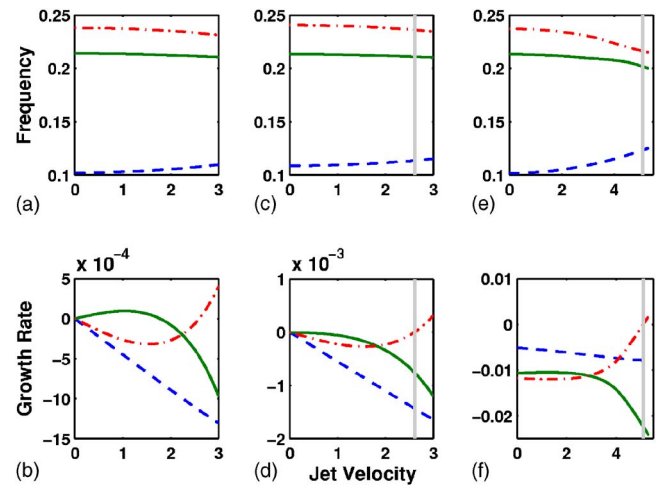


FIG. 11. (Color online) The frequencies and growth rates of the first three eigenmodes (---: first; —: second; -.-: third) as a function of the jet velocity for three cases in which all three flow terms were included ($Q=Q_2\dot{q}+Q_1\dot{q}+Q_0q$). (a-b): model parameters given by Eq. (28), $\sigma=0$; (c-d): model parameters given by Eq. (28) except that $T_{inf}=1.5$, $\sigma=0$; (e-f): model parameters given by Eq. (28), $\sigma=0.1$. The vertical lines indicate point of onset.

turbation introduces a first-order term in time whose matrix coefficient, the flow damping term Q_1 in our case, is no longer positive-definite so that destabilization occurs. In this case, a negative damping was introduced in the second eigenmode and a positive damping in the first and third eigenmodes (Fig. 11(b)). Due to this destabilization effect, the onset of the perturbed system would in general be lower than in the unperturbed system. In our case, the onset jet velocity was decreased to an infinitesimally small number. The destabilization of reversible systems due to irreversible perturbations has been extensively investigated (e.g., Kounadis, 1992; O'Reilly *et al.*, 1996; Kirillov, 2005). O'Reilly *et al.* (1996) examined the destabilization of the equilibria of a reversible system when an infinitesimally small first derivative term in time (the flow damping term in our case) was introduced to the system. Based on the matrix invariants of system governing equations, they established the necessary and sufficient conditions for a two degree-of-freedom system to lose linear stability due to the addition of an irreversible perturbation. Using similar criteria, the eigenvalue movement as shown in Figs. 11(a) and 11(b) can be predicted, i.e., one eigenmode was destabilized while the other stabilized.

For this example without structural damping (Figs. 11(a), 11(b), and 5(c)), since the second eigenmode was destabilized at an infinitesimally small flow velocity, the eigenmodes interacted minimally with each other so that the critical eigenmode was almost the same as the corresponding *in vacuo* eigenmode of the vocal fold structure. Indeed, a close examination showed that the two FSI modes at a very small jet velocity (which is of course slightly beyond onset) were highly similar to the third and the second *in vacuo* eigenmodes of the vocal fold structure, respectively. In fact, the correlation between the FSI-1 mode and the second *in vacuo* eigenmode was above 99%, and the FSI-2 mode was 84% and 53% correlated with the third and first *in vacuo* eigenmodes, respectively. In addition, the FSI-1 mode captured

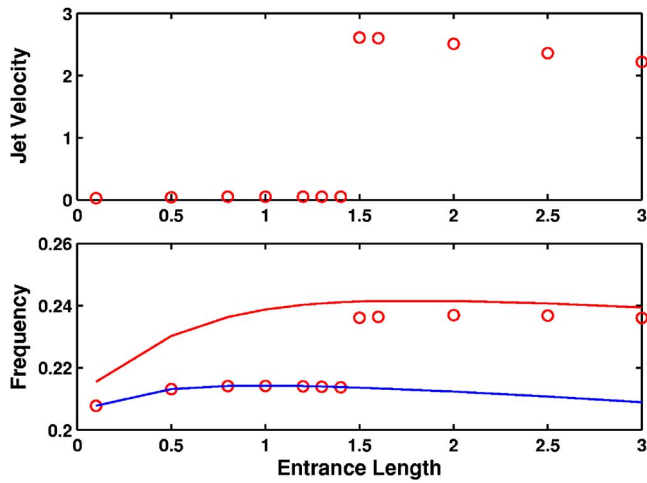


FIG. 12. (Color online) Onset jet velocity (top) and frequency (bottom) as a function of the length of the entrance section T_{inf} , for model parameters given in Eq. (28), $Q = Q_2\dot{q} + Q_1\dot{q} + Q_0q$ for $\sigma = 0$. The two solid lines indicate the second and third *in vacuo* eigenfrequencies.

more than 99% of the total energy. As expected, the critical eigenmode was essentially the second *in vacuo* eigenmode with nearly zero contribution from the other *in vacuo* eigenmodes. The pressure field in the glottal channel and the vocal fold velocity field along the medial surface showed that, for both FSI modes, the pressure fields were in phase with the velocity fields so that the self-mode interaction due to the FSI-1 mode (due to its 99% weight) dominated the total energy flow. In other words, the destabilizing effect of the flow-induced damping is a one-mode instability (the second *in vacuo* eigenmode destabilized by flow-induced damping), as compared to the synchronization of two eigenmodes in Sec. III B.

2. Structure of the Q_1 matrix

The destabilization effect is highly dependent on the structure of the flow damping term Q_1 , which is again dependent on many factors such as the vocal fold geometry. For example, Figs. 11(c) and 11(d) show the frequency and growth rate as a function of the jet velocity for a case with the same conditions as the case in Figs. 11(a) and 11(b), except the length of the entrance section ($z < 0$) of the glottal channel T_{inf} was increased from 1 to 1.5. The first three eigenmodes were all stabilized when the flow was applied, and the system was now linearly stable. Figure 12 shows the onset jet velocity and frequency as a function of the length of the entrance section T_{inf} . A threshold value of T_{inf} (about 1.4) existed above which the onset jet velocity jumped to a finite number. Beyond this threshold, the flow-induced damping became stabilizing so that the system was no longer linearly unstable at very small jet velocities (Fig. 11(d)). Correspondingly, the critical eigenvalue changed from the second to the third eigenvalue, as shown in Fig. 12. Note that the onset jet velocity for values of T_{inf} above the threshold was still much lower than it would have been had the flow-induced damping term been excluded, as discussed further below.

3. Effects of structural damping

The destabilizing effect of the flow-induced damping was suppressed when structural damping was included to the coupled system. Figures 11(e) and 11(f) show the frequency and growth rate as a function of the jet velocity for the same case as in Figs. 11(a) and 11(b) but with a loss factor of 0.1. The corresponding movement of the second and third eigenvalues in the complex half plane is shown in Fig. 5(d). When a nonzero flow was applied, the second and third eigenvalues started in opposite directions, under the influence of the flow-induced damping. As the jet velocity increased, the two eigenvalues eventually reversed directions under the influence of the flow stiffness term. The system remained stable until the jet velocity reached a finite value. As the jet velocity further increased, the flow stiffness term dominated and eventually destabilized the coupled system (onset). Although a relatively large loss factor (0.1) was used in this example, a much smaller loss factor would also suppress the destabilizing effect of the flow-induced damping, as discussed later. For moderate and high structural damping, the effects of the flow-induced damping on phonation onset became secondary, and the onset was again primarily determined by the properties of the flow-induced stiffness matrix, as discussed in Sec. III B.

However, similar to that of the structural damping (Sec. III B 4) but to a much larger extent, the presence of the flow damping term destroyed the interaction between the second and third eigenvalues, which would have collided on the imaginary axis and led to onset as in Sec. III B. Phonation onset occurred well before the eigenvalues sufficiently approximated each other (compare with Figs. 5(a) and 5(b)). In fact, the two eigenvalues only minimally approached each other in the complex half plane and never collided.

Figure 10 shows the onset jet velocity and onset frequency (denoted by square symbols) as a function of the loss factor for the model parameters specified by Eq. (28), with all three terms of the flow pressure included in Eq. (22). At a very small value of the loss factor, the onset jet velocity jumped from an infinitesimally small one (not shown in Fig. 10) to finite values (about 3). After that, the onset jet velocity increased smoothly with increasing loss factor, as in the case when only flow stiffness was included. Compared to the case with only the flow stiffness term included, two regions of the loss factor can be identified. For loss factors smaller than about 0.06, the onset jet velocity was lowered when the flow damping was added due to the destabilizing effect of the flow damping term. For loss factors larger than 0.06, the onset jet velocity was higher when the flow damping term was included. Obviously, the flow-induced damping changed from destabilizing to stabilizing at large structural damping.

Figure 13 shows the correlations between the two FSI modes and the first four *in vacuo* eigenmodes, the relative energy weights of the two FSI modes, and the energy flow decomposition as a function of the loss factor, for cases in which all three terms of the flow pressure were included in Eq. (22). Similar observations can be made as those in Sec. III B 4. Both FSI modes were a mixture of the first three *in vacuo* eigenmodes of the vocal folds. For small and moderate structural damping, the FSI-1 mode captured an out-of-

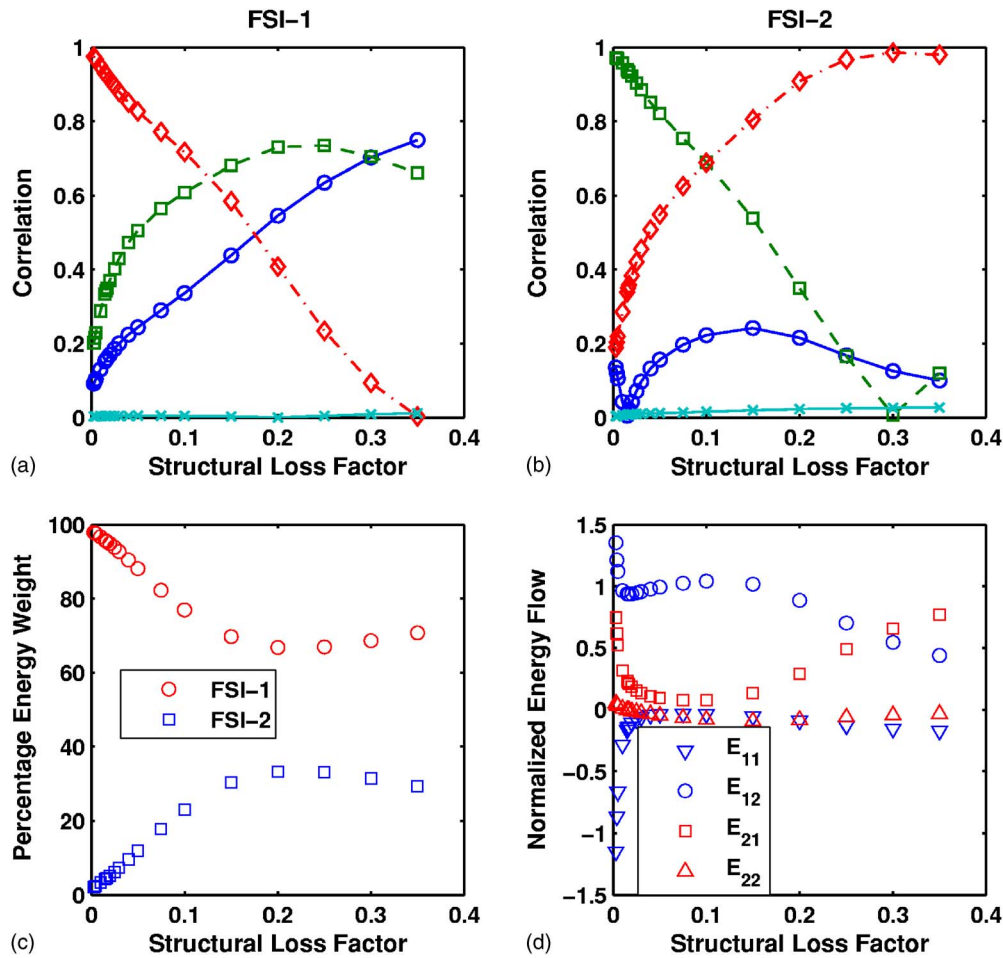


FIG. 13. (Color online) Correlation between the FSI-1 mode (a) and FSI-2 mode (b) and the first four *in vacuo* eigenmodes (\circ : first; \square : second; \diamond : third; \times : fourth *in vacuo* eigenmodes), relative energy weights of the two FSI modes (c), and normalized contributions to the total energy flow by individual interaction terms (d) as a function of the structural loss factor. Model parameters were given in Eq. (28), $Q = Q_2\dot{q} + Q_1\dot{q} + Q_0q$.

phase lateral motion, while the FSI-2 mode captured an in-phase lateral motion. The vibration patterns changed around $\sigma=0.25$ so that, for higher structural damping, the FSI-1 captured an in-phase lateral motion while the FSI-2 mode captured an out-of-phase motion. The value of the loss factor at the switchover was not much different from the case when only the flow stiffness term was included. As the structural damping increased, the relative weight of the FSI-1 mode decreased while that of the FSI-2 mode increased. Note that for moderate to high structural damping, the relative weights of the two FSI modes (about 70% and 30%, respectively) were similar to those of the surface-based empirical eigenfunctions observed in laboratory experiments (Berry *et al.*, 2001; Zhang *et al.*, 2006b). Concerning the energy transfer mechanism, as the structural damping increased, the pattern of energy flow decomposition approached that of the case when only flow stiffness was included. That is, the dominant contribution to the total energy transfer came from the interaction between the pressure field induced by the out-of-phase FSI mode and the vocal fold motion of the in-phase FSI mode.

IV. DISCUSSION

In this study, the primary mechanism of phonation onset was flow-induced stiffness, rather than flow-induced damp-

ing. In particular, the asymmetric nature of the flow-induced stiffness matrix induced two neighboring eigenvalues to approximate each other and eventually merge, initiating phonation onset. In this study, the asymmetry of the flow-induced stiffness matrix was mainly caused by flow separation. However, such an asymmetry may also be induced by other non-conservative mechanisms such as viscous flow resistance. Only under conditions of negligible structural damping and a restricted set of vocal fold geometries did flow-induced damping become the primary mechanism of phonation. At moderate to high structural damping, although phonation onset was not directly related to an eigenmode-synchronization, the primary mechanism of phonation onset remained to be the synchronization effect of the flow-induced stiffness.

Some of the initial results of this investigation closely parallel the linear stability analysis of the two-mass model performed by Ishizaka and colleagues (Ishizaka and Matsu-daira, 1972; Ishizaka, 1981, 1988), particularly with respect to the role of the flow-induced stiffness term in facilitating eigenmode synchronization and initiating phonation. These studies underscore the necessity of retaining at least two degrees-of-freedom in lumped-element models of phonation. For a single degree-of-freedom system (e.g., the one-mass model or any degenerate two-mass model), eigenmode synchronization mechanism is excluded *a priori*. For example,

in the one-mass model, the only mechanism of phonation relies on externally introduced damping (e.g., by coupling to an acoustic resonance). Without externally introduced damping, only a static divergence instability (due to the interaction between the single eigenvalue with its complex conjugate) is possible in a single degree-of-freedom system.

It is difficult to compare the results of the present investigation with results of Titze (1988). In part, this is because the present study used a self-oscillating, two-dimensional, fluid-structure interaction system, while Titze (1988) used a two degree-of-freedom system with prescribed phase relationship between the two eigenmodes. Therefore, while Titze (1988) investigated the consequences of eigenmode synchronization, he failed to investigate the mechanisms of eigenmode synchronization. In particular, Titze (1988) showed that the synchronization of two structural eigenmode produced an effective negative damping term in the resulting single degree-of-freedom system. However, this concept of negative damping provides no insight regarding how eigenmode synchronization might be initiated and facilitated by the aeroelastic properties of the coupled fluid-structure-interaction system. Furthermore, the concept of modeling eigenmode synchronization as an effective negative damping, similar to the flow-induced damping introduced by sub- and supra-glottal acoustics (Titze, 1988; Zhang *et al.*, 2006a), may be misleading. Indeed, the present study shows that flow-induced stiffness, rather than flow-induced damping, was the primary mechanism of both phonation onset and eigenmode synchronization, except for one exceptional case.

For the results presented thus far, phonation onset generally occurred due to the synchronization of two closely spaced *in vacuo* eigenvalues. However, in other cases not reported in this study, the eigenvalues which ultimately synchronized were not necessarily closely spaced in the *in vacuo* state. For example, for a slightly different vocal fold geometry, as we varied the flow separation point superiorly along the vocal fold medial surface, the two eigenmodes which synchronized switched from the first and second eigenmodes, to the second and third, and then back to the first and second eigenmodes. Depending on the degree of asymmetry of the flow-induced stiffness matrix, the system sometimes lost stability to a static divergence. Future studies with more comprehensive evaluations over the entire phonatory range are needed to probe the influence of flow parameters (in particular flow separation location) on the movement of the eigenvalues and the factors determining which eigenmodes interact to induce phonation onset.

The linear stability analysis in this study was simplified by a few assumptions which should be relaxed in future studies. First of all, as mentioned in Sec. II, the steady-state problem of the coupled system should be solved for each subglottal pressure. This will give the deformed shape of the vocal folds and the glottal channel based on which the linear stability analysis is performed, and allows the effects of the mean deformation to be investigated. Second, the flow model used in this model was based on one-dimensional potential flow theory and viscous effects were mostly excluded. This means that the conclusions made in this study may not be valid for limiting conditions, such as vanishing structural

damping and an extremely small glottal gap width. The one-dimensional flow description might over simplify the glottal flow dynamics, especially when coupled with a two-dimensional structure model. Other assumptions of the flow such as the fixed flow separation point and zero pressure recovery beyond flow separation should also be relaxed. A more realistic description of the flow, such as the Navier-Stokes equations, should be used instead. The linear stability analysis should then be repeated combining the Navier-Stokes flow with a continuum structure model. On the structural side, a major assumption made in this study was the linear stress-strain relationship of the vocal fold, a condition under which the mean stress and strain in the vocal fold structure can be neglected. When the nonlinearity of the vocal fold material properties is included, the equilibrium stress and strain of the vocal fold structure can no longer be neglected from the linearized equations and therefore have to be solved prior to the linear stability analysis. Of course, a nonlinear stress-strain relationship would also affect the equilibrium geometry of the vocal fold, around which the system equations are linearized.

The analysis of this study can be easily extended to a three-dimensional full vocal folds model so that asymmetric phenomena (asymmetry in the vibration pattern or asymmetry of the glottal flow, e.g., Neubauer *et al.*, 2001, 2007) and three-dimensional effects can be studied. The subglottal and supraglottal acoustics, which are known to be another mechanism of energy transfer, also can be included in the model by using appropriate impedance boundary conditions for the superior and inferior ends of the glottal channel (Sec. II B). These topics will be explored in future studies.

This study shows that the two FSI modes at onset can be expressed as a linear combination of the first four *in vacuo* eigenmodes with reasonable accuracy. The two FSI modes also exhibited a high correlation with the empirical eigenfunctions (EEFs) extracted from medial surface dynamics of the vocal folds (Appendix), indicating that the EEFs could be also expressed as a linear combination of a few *in vacuo* eigenmodes within certain accuracy. These eigenmodes (either the two FSI modes expressed in terms *in vacuo* eigenmodes, or the EEFs) may be used as basis functions for vocal fold modeling. Reduced order models can therefore be obtained for the vocal folds by projecting the governing equations of the vocal folds onto these basis functions. Further, by combining these structural eigenmodes with empirical eigenfunctions of the glottal flow, reduced order models may be developed for a coupled fluid-structure system of phonation (Dowell and Hall, 2001). These reduced order models would allow the system dynamics to be represented by a few dominant eigenmodes, and therefore greatly reduce the computational requirement, which makes it possible for these models to be used in practical applications (e.g., clinic voice diagnosis or prediction of voice surgery outcome).

V. CONCLUSIONS

In this study, we investigated the linear stability of a two-dimensional continuum model of the vocal folds coupled with a potential glottal flow for a fixed flow separa-

tion point. We showed that the primary aerodynamic mechanism of phonation onset was the flow-induced stiffness, rather than flow-induced damping. The asymmetric nature of the flow-induced stiffness, caused by nonconservative factors such as flow separation or viscous flow resistance, induced a cross-mode coupling effect. Due to this coupling effect, two *in vacuo* eigenvalues of the vocal fold approximated each other in the complex plane and, at onset, collided with each other to produce an unstable eigenmode. The synchronization of the two eigenmodes provided a net energy transfer from the airflow to the vocal fold structure to overcome the structural dissipation. Only under conditions of negligible structural damping and a restricted set of vocal fold geometries did flow-induced damping become the primary mechanism of phonation onset. However, for moderate to high structural damping, the flow-induced stiffness remained the primary aerodynamic mechanism of phonation onset.

ACKNOWLEDGMENTS

This study was supported by Grant No. R01 DC004688 from the National Institute on Deafness and Other Communication Disorders, the National Institutes of Health.

APPENDIX: VOLUME-BASED AND SURFACE-BASED EIGENFUNCTIONS OF VOCAL FOLD VIBRATION

In this study the two spatially and temporally orthogonal FSI modes were extracted based on the vibration dynamics of the entire vocal fold volume. In previous experiments, empirical eigenfunctions (EEFs) were extracted from the observed motion of the vocal fold medial surface. The principal component analysis (PCA) was used in both methods of decomposition, but on data of different domain. The two FSI modes are volume-based eigenfunctions and orthogonal in terms of the whole vocal fold volume, while the EEFs are surface based and orthogonal only along the vocal fold surface. To investigate the possible correlations between these two methods of decomposition, a spatio-temporal dataset of the vocal fold displacement along the vocal fold surface was generated using the critical eigenvector at onset for one case with model parameters specified in Eq. (28) and with a loss factor of 0.1. Empirical eigenfunctions were then extracted from this surface displacement data using the principal component analysis. The first two EEFs were found to be enough to reproduce the whole dynamics, each capturing 87.8% and 12.2% of the total energy, respectively. These compare to the relative energy weights of 76.9% and 23.1% for the FSI-1 and the FSI-2 modes, respectively. Figure 14 compares the first two EEFs (left half of each subfigure) and the two FSI modes (right half in each subfigure). The EEFs were almost the same as the two FSI modes, except for a slight difference between the second EEF and the FSI-2 mode. These differences were further quantified by calculating the surface-based dot product (vector product in Eq. (27) without the M matrix) between the two sets of eigenfunctions. The correlation between the FSI-1 mode and the first EEF was 99.9%, while the correlation between the FSI-2 mode and the second EEF was 98.1%. Although the two sets of eigenfunctions were generated based on different input data, they were

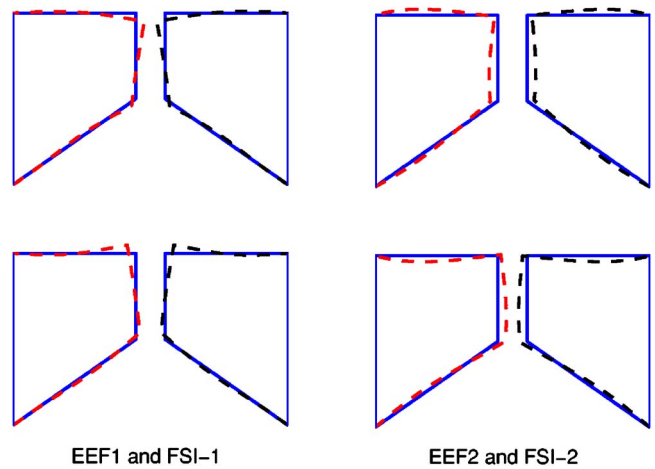


FIG. 14. (Color online) Comparison between the two FSI modes and the first two EEFs of the vibration dynamics along the vocal fold surface. In each subfigure, the left half is the EEF while the right half is the FSI mode. —: equilibrium positions; - - : maximum or minimum displacement of the eigenfunctions superimposed on the equilibrium projections. Model parameters given in Eq. (28), $Q=Q_2\dot{q}+Q_1\dot{q}+Q_0q$, $\sigma=0.1$.

highly similar in terms of vibration patterns and only slightly different in terms of relative energy weights. This high correlation is probably due to the fact that the vocal fold in this case was nearly incompressible ($\nu=0.47$, Eq. (28)).

- Auregan, Y., and Depollier, C. (1995). "Snoring: linear stability analysis and *in-vitro* experiments," *J. Sound Vib.* **188**, 39–54.
- Benjamin, T. B. (1960). "Effects of a flexible boundary on hydrodynamic stability," *J. Fluid Mech.* **9**, 513–532.
- Benjamin, T. B. (1963). "The threefold classification of unstable disturbances in flexible surfaces bounding inviscid flows," *J. Fluid Mech.* **16**, 436–450.
- Berry, D. A., Herzel, H., Titze, I. R., and Krischer, K. (1994). "Interpretation of biomechanical simulations of normal and chaotic vocal fold oscillations with empirical eigenfunctions," *J. Acoust. Soc. Am.* **95**, 3595–3604.
- Berry, D. A., Montequin, D. W., and Tayama, N. (2001). "High-speed digital imaging of the medial surface of the vocal folds," *J. Acoust. Soc. Am.* **110**, 2539–2547.
- Berry, D. A., and Titze, I. R. (1996). "Normal modes in a continuum model of vocal fold tissues," *J. Acoust. Soc. Am.* **100**, 3345–3354.
- Berry, D. A., Zhang, Z., and Neubauer, J. (2006). "Mechanisms of irregular vibration in a physical model of the vocal folds," *J. Acoust. Soc. Am.* **120**(3), EL36–EL42.
- Carpenter, P. W., and Garrad, A. D. (1985). "The hydrodynamic stability of flow over Kramer-type compliant surfaces. Part 1. Tollmien-Schlichting instabilities," *J. Fluid Mech.* **155**, 465–510.
- Carpenter, P. W., and Garrad, A. D. (1986). "The hydrodynamic stability of flow over Kramer-type compliant surfaces. Part 2. Flow-induced surface instabilities," *J. Fluid Mech.* **170**, 199–232.
- Cook, D., and Mongeau, L. (2007). "Sensitivity of a continuum vocal fold model to geometric parameters, constraints, and boundary conditions," *J. Acoust. Soc. Am.* **121**, 2247–2253.
- Cullen, J. S., Gilbert, J., and Campbell, D. M. (2000). "Brass instruments: Linear stability analysis and experiments with an artificial mouth," *Acustica* **86**, 704–724.
- Deverge, M., Pelorson, X., Vilain, C., Lagree, P. Y., Chentouf, F., Willems, J., and Hirschberg, A. (2003). "Influence of collision on the flow through *in-vitro* rigid models of the vocal folds," *J. Acoust. Soc. Am.* **114**, 3354–3362.
- Dowell, E. H., and Hall, K. C. (2001). "Modeling of fluid-structure interaction," *Annu. Rev. Fluid Mech.* **33**, 445–490.
- Duncan, J. H. (1987). "A comparison of wave propagation on the surfaces of simple membrane walls and elastic coatings bounded by a fluid flow," *J. Sound Vib.* **119**, 565–573.
- Flanagan, J. L., and Landgraf, L. L. (1968). "Self oscillating source for

- vocal tract synthesizers," *IEEE Trans. Audio Electroacoust.* **16**, 57–64.
- Grotberg, J. B., and Jensen, O. E. (2004). "Biofluid mechanics in flexible tubes," *Annu. Rev. Psychol.* **36**, 121–147.
- Guckenheimer, J., and Holmes, P. (1983). *Nonlinear Oscillations, Dynamical Systems, and Bifurcation of Vector Fields* (Springer-Verlag, New York).
- Holmes, P. J. (1977). "Bifurcations to divergence and flutter in flow-induced oscillations: A finite dimensional analysis," *J. Sound Vib.* **53**(4), 471–503.
- Holmes, P., Lumley, J. L., and Berkooz, G. (1996). *Turbulence, Coherent Structures and Symmetry* (Cambridge University Press, Cambridge, UK).
- Horacek, J., and Svec, J. G. (2002). "Aeroelastic model of vocal-fold-shaped vibrating element for studying the phonation threshold," *J. Fluids Struct.* **16**(7), 931–955.
- Huang, L. (2001). "Viscous flutter of a finite elastic membrane in poiseuille flow," *J. Fluids Struct.* **15**, 1061–1088.
- Ishizaka, K. (1981). "Equivalent lumped-mass models of vocal fold vibration," in *Vocal Fold Physiology*, edited by K. N. Stevens and M. Hirano (University of Tokyo, Tokyo), pp. 231–244.
- Ishizaka, K. (1988). "Significance of Kaneko's measurement of natural frequencies of the vocal folds," in *Vocal Physiology: Voice Production, Mechanisms and Functions*, edited by Osamu Fujimara (Raven, New York), pp. 181–190.
- Ishizaka, K., and Flanagan, J. L. (1972). "Synthesis of voiced sounds from a two-mass model of the vocal cords," *Bell Syst. Tech. J.* **51**, 1233–1267.
- Ishizaka, K., and Matsudaira, M. (1972). "Fluid mechanical considerations of vocal cord vibration," *Monogr. 8, Speech Commun. Res. Lab., Santa Barbara, CA*.
- Kirillov, O. N. (2005). "A theory of the destabilization paradox in non-conservative systems," *Acta Mech.* **174**, 145–166.
- Kounadis, A. N. (1992). "On the paradox of the destabilizing effect of damping in non-conservative systems," *Int. J. Non-Linear Mech.* **27**(4), 597–609.
- Landahl, M. T. (1962). "On the stability of a laminar incompressible boundary layer over a flexible surface," *J. Fluid Mech.* **13**, 609–632.
- Lighthill, M. J. (1978). *Waves in Fluids* (Cambridge University Press, New York).
- Lucey, A. D., and Carpenter, P. W. (1993). "The hydroelastic stability of three-dimensional disturbances of a finite compliant wall," *J. Sound Vib.* **165**, 527–552.
- Luo, X. Y., and Pedley, T. J. (1996). "A numerical simulation of unsteady flow in a two-dimensional collapsible channel," *J. Fluid Mech.* **314**, 191–225.
- Matsuzaki, Y., and Fung, Y. C. (1977). "Stability analysis of straight and buckled two-dimensional channels conveying an incompressible flow," *J. Appl. Mech.* **44**, 548–552.
- Matsuzaki, Y., and Fung, Y. C. (1979). "Non-linear stability analysis of a two-dimensional model of an elastic tube conveying a compressible flow," *J. Appl. Mech.* **46**, 31–36.
- Neubauer, J., Mergell, P., Eysholdt, U., and Herzel, H. (2001). "Spatio-temporal analysis of irregular vocal fold oscillations: Biphonation due to desynchronization of spatial modes," *J. Acoust. Soc. Am.* **110**, 3179–3192.
- Neubauer, J., Zhang, Z., Miraghaie, R., and Berry, D. A. (2007). "Coherent structures of the near field flow in a self-oscillating physical model of the vocal folds," *J. Acoust. Soc. Am.* **121**, 1102–1118.
- O'Reilly, O. M., Malhotra, N. K., and Namachchivaya, N. S. (1996). "Some aspects of destabilization in reversible dynamical systems with application to follower forces," *Nonlinear Dyn.* **10**, 63–87.
- Pierucci, M. (1977). "Surface waves of an elastic medium in the presence of an inviscid flow field," *J. Acoust. Soc. Am.* **61**, 965–971.
- Steinecke, I., and Herzel, H. (1995). "Bifurcations in an asymmetric vocal fold model," *J. Acoust. Soc. Am.* **97**, 1874–1884.
- Story, B. H., and Titze, I. R. (1995). "Voice simulation with a body-cover model of the vocal folds," *J. Acoust. Soc. Am.* **97**, 1249–1260.
- Titze, I. R. (1988). "The physics of small-amplitude oscillation of the vocal folds," *J. Acoust. Soc. Am.* **83**(4), 1536–1552.
- Titze, I. R., Schmidt, S. S., and Titze, M. R. (1995). "Phonation threshold pressure in a physical model of the vocal fold mucosa," *J. Acoust. Soc. Am.* **97**, 3080–3084.
- Titze, I. R., and Strong, W. J. (1975). "Normal modes in vocal cord tissues," *J. Acoust. Soc. Am.* **57**, 736–744.
- Weaver, D. S. (1974). "On the non-conservative nature of "Gyroscopic conservative" systems," *J. Sound Vib.* **36**, 435–437.
- Williamson, C. H. K., and Govardhan, R. (2004). "Vortex-induced vibrations," *Annu. Rev. Fluid Mech.* **36**, 413–455.
- Yeo, K. S., (1988). "The stability of boundary-layer flow over single- and multi-layer viscoelastic walls," *J. Fluid Mech.* **196**, 359–408.
- Yeo, K. S., (1992). "The three-dimensional stability of boundary-layer flow over compliant walls," *J. Fluid Mech.* **238**, 537–577.
- Yeo, K. S., Khoo, B. C., and Chong, W. K. (1994). "The linear stability of boundary-layer flow over compliant walls - the effects of the wall mean state, induced by flow loading," *J. Fluids Struct.* **8**, 529–551.
- Zhang, Z., Neubauer, J., and Berry, D. A. (2006a). "The influence of subglottal acoustics on laboratory models of phonation," *J. Acoust. Soc. Am.* **120**(3), 1558–1569.
- Zhang, Z., Neubauer, J., and Berry, D. A. (2006b). "Aerodynamically and acoustically driven modes of vibration in a physical model of the vocal folds," *J. Acoust. Soc. Am.* **120**(5), 2841–2849.